EMPRESS. XII. Statistics on the Dynamics and Gas Mass Fraction of Extremely Metal-poor Galaxies

Yi Xu[1,2], Masami Ouchi[1,3,4], Yuki Isobe[1,5], Kimihiko Nakajima[3], Shinobu Ozaki[3], Nicolas F. Bouché[6], John H. Wise[7], Eric Emsellem[6,8], Haruka Kusakabe[9], Takashi Hattori[10], Tohru Nagao[11], Gen Chiaki[3], Hajime Fukushima[12], Yuichi Harikane[1,13], Kohei Hayashi[1,14,15], Yutaka Hirai[15,16], Ji Hoon Kim[17,18], Michael V. Maseda[19], Kentaro Nagamine[4,20,21], Takatoshi Shibuya[22], Yuma Sugahara[3,23], Hidenobu Yajima[12], Shohei Aoyama[1,24], Seiji Fujimoto[1,3,25,26,27], Keita Fukushima[20], Shun Hatano[28], Akio K. Inoue[23,29], Tsuyoshi Ishigaki[30], Masahiro Kawasaki[1,4], Takashi Kojima[1,5], Yutaka Komiyama[31], Shuhei Koyama[32], Yusei Koyama[10,28], Chien-Hsiu Lee[33], Akinori Matsumoto[1,5], Ken Mawatari[3], Takashi J. Moriya[3,34], Kentaro Motohara[3,32], Kai Murai[1], Moka Nishigaki[3,28], Masato Onodera[10,28], Yoshiaki Ono[1], Michael Rauch[35], Tomoki Saito[36], Rin Sasaki[30], Akihiro Suzuki[37], Tsutomu T. Takeuchi[38,39], Hiroya Umeda[1,5], Masayuki Umemura[12], Kuria Watanabe[28], Kiyoto Yabe[4], and Yechi Zhang[1,5]

[1] Institute for Cosmic Ray Research, The University of Tokyo, 5-1-5 Kashiwanoha, Kashiwa, Chiba 277-8582, Japan; xuyi@icrr.u-tokyo.ac.jp
[2] Department of Astronomy, Graduate School of Science, The University of Tokyo, 7-3-1 Hongo, Bunkyo, Tokyo 113-0033, Japan
[3] National Astronomical Observatory of Japan, 2-21-1 Osawa, Mitaka, Tokyo 181-8588, Japan
[4] Kavli Institute for the Physics and Mathematics of the Universe (WPI), The University of Tokyo, Kashiwa, Chiba 277-8583, Japan
[5] Department of Physics, Graduate School of Science, The University of Tokyo, 7-3-1 Hongo, Bunkyo, Tokyo 113-0033, Japan
[6] Université Lyon, Université Lyon1, ENS de Lyon, CNRS, Centre de Recherche Astrophysique de Lyon UMR5574, F-69230 Saint-Genis-Laval France
[7] Center for Relativistic Astrophysics, School of Physics, Georgia Institute of Technology, Atlanta, GA 30332, USA
[8] European Southern Observatory, Karl-Schwarzschild-Straße 2, D-85748 Garching, Germany
[9] Observatoire de Genéve, Université de Genève, 51 Ch. des Maillettes, 1290 Versoix, Switzerland
[10] Subaru Telescope, National Astronomical Observatory of Japan, National Institutes of Natural Sciences (NINS), 650 North A'ohoku Place, Hilo, HI 96720, USA
[11] Research Center for Space and Cosmic Evolution, Ehime University, Bunkyo-cho 2-5, Matsuyama, Ehime 790-8577, Japan
[12] Center for Computational Sciences, University of Tsukuba, Ten-nodai, 1-1-1 Tsukuba, Ibaraki 305-8577, Japan
[13] Department of Physics and Astronomy, University College London, Gower Street, London WC1E 6BT, UK
[14] National Institute of Technology, Ichinoseki College, Hagisho, Ichinoseki, 021-8511, Japan
[15] Astronomical Institute, Tohoku University, 6-3 Aoba, Aramaki, Aoba-ku, Sendai, Miyagi 980-8578, Japan
[16] Department of Physics and Astronomy, University of Notre Dame, 225 Nieuwland Science Hall, Notre Dame, IN 46556, USA
[17] Astronomy Program, Department of Physics and Astronomy, Seoul National University, 1 Gwanak-ro, Gwanak-gu, Seoul 08826, Republic of Korea
[18] SNU Astronomy Research Center, Seoul National University, 1 Gwanak-ro, Gwanak-gu, Seoul 08826, Republic of Korea
[19] Department of Astronomy, University of Wisconsin–Madison, 475 N. Charter Street, Madison, WI 53706, USA
[20] Theoretical Astrophysics, Department of Earth & Space Science, Graduate School of Science, Osaka University, 1-1 Machikaneyama, Toyonaka, Osaka 560-0043, Japan
[21] Department of Physics & Astronomy, University of Nevada, Las Vegas, 4505 S. Maryland Parkway, Las Vegas, NV 89154-4002, USA
[22] Kitami Institute of Technology, 165 Koen-cho, Kitami, Hokkaido 090-8507, Japan
[23] Waseda Research Institute for Science and Engineering, Faculty of Science and Engineering, Waseda University, 3-4-1, Okubo, Shinjuku, Tokyo 169-8555, Japan
[24] Institute of Management and Information Technologies, Chiba University, 1-33, Yayoi-cho, Inage-ward, Chiba, 263-8522, Japan
[25] Cosmic Dawn Center (DAWN), Jagtvej 128, DK-2200 Copenhagen N, Denmark
[26] Niels Bohr Institute, University of Copenhagen, Lyngbyvej2, DK-2100, Copenhagen, Denmark
[27] Research Institute for Science and Engineering, Waseda University, 3-4-1 Okubo, Shinjuku, Tokyo 169-8555, Japan
[28] Department of Astronomical Science, SOKENDAI (The Graduate University for Advanced Studies), Osawa 2-21-1, Mitaka, Tokyo, 181-8588, Japan
[29] Department of Physics, School of Advanced Science and Engineering, Faculty of Science and Engineering, Waseda University, 3-4-1 Okubo, Shinjuku, Tokyo 169-8555, Japan
[30] Department of Physical Science and Materials Engineering, Faculty of Science and Engineering, Iwate University 3-18-34 Ueda, Morioka, Iwate 020-8550, Japan
[31] Department of Advanced Sciences, Faculty of Science and Engineering, Hosei University, 3-7-2 Kajino-cho, Koganei-shi, Tokyo 184-8584, Japan
[32] Institute of Astronomy, Graduate School of Science, The University of Tokyo, 2-21-1 Osawa, Mitaka, Tokyo 181-0015, Japan
[33] W.M. Keck Observatory, Kamuela, HI 96743, USA
[34] School of Physics and Astronomy, Faculty of Science, Monash University, Clayton, Victoria 3800, Australia
[35] Carnegie Observatories, 813 Santa Barbara Street, Pasadena, CA 91101, USA
[36] Nishi-Harima Astronomical Observatory, Centre for Astronomy, University of Hyogo, 407-2 Nishigaichi, Sayo, Sayo-gun, Hyogo 679-5313, Japan
[37] Research Center for the Early Universe, The University of Tokyo, 7-3-1 Hongo, Bunkyo, Tokyo 113-0033, Japan
[38] Division of Particle and Astrophysical Science, Nagoya University, Furo-cho, Chikusa-ku, Nagoya 464-8602, Japan
[39] The Research Center for Statistical Machine Learning, The Institute of Statistical Mathematics, 10-3 Midori-cho, Tachikawa, Tokyo 190-8562, Japan

Abstract

We present the demography of the dynamics and gas mass fraction of 33 extremely metal-poor galaxies (EMPGs) with metallicities of 0.015–0.195 $Z_\odot$ and low stellar masses of 10^4–$10^8\,M_\odot$ in the local universe. We conduct deep optical integral field spectroscopy (IFS) for the low-mass EMPGs with the medium-high resolution ($R = 7500$) grism of the 8 m Subaru FOCAS IFU instrument by the EMPRESS 3D survey, and investigate the Hα emission of

the EMPGs. Exploiting the resolution high enough for the low-mass galaxies, we derive gas dynamics with the Hα lines by the fitting of three-dimensional disk models. We obtain an average maximum rotation velocity ($v_{\rm rot}$) of $15 \pm 3 \, {\rm km \, s}^{-1}$ and an average intrinsic velocity dispersion (σ_0) of $27 \pm 10 \, {\rm km \, s}^{-1}$ for 15 spatially resolved EMPGs out of 33 EMPGs, and find that all 15 EMPGs have $v_{\rm rot}/\sigma_0 < 1$ suggesting dispersion-dominated systems. There is a clear decreasing trend of $v_{\rm rot}/\sigma_0$ with the decreasing stellar mass and metallicity. We derive the gas mass fraction ($f_{\rm gas}$) for all 33 EMPGs, and find no clear dependence on stellar mass and metallicity. These $v_{\rm rot}/\sigma_0$ and $f_{\rm gas}$ trends should be compared with young high-z galaxies observed by the forthcoming JWST IFS programs to understand the physical origins of the EMPGs in the local universe.

Unified Astronomy Thesaurus concepts: Galaxy evolution (594); Galaxy kinematics (602); Galaxy dynamics (591); Dwarf galaxies (416)

1. Introduction

Classical galaxy formation theory suggests galaxy initially forms as angular-momentum-supported disks (White & Rees 1978; Fall & Efstathiou 1980; Blumenthal et al. 1984). Primordial galaxies evolve into the various types of galaxies we see today involving a complex interplay between different processes: accretion of cold gas, minor and major mergers, and stellar and active galactic nuclei feedback. One way to understand the evolution of primordial galaxies and the complex interplay is to study the dynamics of high-z galaxies. Rizzo et al. (2020, 2021) analyze the kinematics of $z \sim 4$–5 galaxies and obtain a large maximum rotation velocity ($v_{\rm rot}$) that is ~ 10 times the velocity dispersion (σ_0). Tokuoka et al. (2022) identify a $z \sim 9$ galaxy that possibly presents clear rotation. Given that galaxies in Rizzo et al. (2020) and Tokuoka et al. (2022) reside in low-mass dark matter (DM) halos with halo masses of $\sim 10^{10}$ and $\sim 10^9 \, M_\odot$, respectively, the disk structure may not be stable but is easily disrupted by inflow or outflow. Simulations of Dekel et al. (2020) suggest a critical DM halo mass of $M_{\rm h} < 2 \times 10^{11} \, M_\odot$, below which the disk cannot survive and the galaxy becomes dispersion dominated.

Although the dynamics of high-z galaxies can be investigated with state-of-the-art observation facilities (e.g., JWST), local dwarf galaxies with recent starbursts are also important test beds of galaxy evolution theories due to their apparent brightness. Local galaxies are advantageous for conducting deep observations with high spectral and spatial resolutions, such as optical integral field spectroscopy (IFS). The spatially resolved Hα recombination line can be used to trace the kinematics of ionized gas (e.g., Green et al. 2014; Barat et al. 2020). Among local dwarf galaxies, extremely metal-poor galaxies (EMPGs) are considered local counterparts of high-z primordial galaxies having gas-phase metallicity (hereafter metallicity) below 10% $Z_\odot$. EMPGs typically have low stellar masses $\lesssim 10^8 \, M_\odot$ and high specific star formation rates (sSFRs) $\gtrsim 1 \, {\rm Gyr}^{-1}$ suggestive of shallow gravitational potential and recent starburst, respectively. Kinematics of EMPGs can provide us a hint of the important mechanism (e.g., inflow/outflow) during the early stage of galaxy formation. Despite that EMPGs may differ from primordial galaxies on numerous aspects (star formation histories, stellar population, etc.), we aim to provide a clear correlation between dynamics and metallicity/stellar mass that can be extrapolated to high-z primordial galaxies. Two important quantities indicating the detailed gas dynamical state are the relative level of rotation, via the $v_{\rm rot}/\sigma_0$ ratio, and the mass composition, via the gas mass fraction ($f_{\rm gas}$).

Recently, the project Extremely Metal-Poor Representatives Explored by the Subaru Survey (EMPRESS) has been launched (Kojima et al. 2020, hereafter Paper I). EMPRESS aims to select faint EMPG photometric candidates from Subaru/Hyper Suprime-Cam (HSC; Miyazaki et al. 2018) deep optical ($i_{\rm lim} = 26$ mag; Aihara et al. 2019) images, which are 2 dex deeper than those of the Sloan Digital Sky Survey (SDSS). Conducting follow-up spectroscopic observations of the EMPG photometric candidates, EMPRESS has identified new 12 EMPGs with low stellar masses of $10^{4.2}$–$10^{6.6} \, M_\odot$ (Paper I, Isobe et al. 2022, hereafter Paper IV; Nakajima et al. 2022, hereafter Paper V; Xu et al. 2022, hereafter Paper VI). Remarkably, J1631+4426 has been reported to have a metallicity of 0.016 $Z_\odot$, which is the lowest metallicity identified so far (Paper I; see Thuan et al. 2022).

This paper is the 12th paper of EMPRESS, reporting a demography of Hα kinematics of EMPGs observed with Subaru/Faint Object Camera and Spectrograph (FOCAS) IFU (Ozaki et al. 2020) in a series of the Subaru Intensive Program entitled EMPRESS 3D (PI: M. Ouchi). So far, EMPRESS has released eight papers related to EMPGs, each of which reports the survey design (Paper I), high Fe/O ratios suggestive of massive stars (Kojima et al. 2021, hereafter Paper II; Paper IV), morphology (Isobe et al. 2021, hereafter Paper III), low-Z ends of metallicity diagnostics (Paper V), outflows (Paper VI), the shape of incident spectrum that reproduces high ionization lines (Umeda et al. 2022, hereafter Paper VII), the primordial He abundance (Matsumoto et al. 2022, hereafter Paper VIII), and the pioneering results of Hα kinematics (Isobe et al. 2023, hereafter Paper IX).

The paper is structured as follows. Section 2 explains our observations and data set. Section 3 describes how we derive rotation velocity, velocity dispersion, and gas mass fraction. We discuss and summarize our findings in Sections 4 and 5, respectively. Throughout the paper, we assume a solar metallicity of $12 + \log({\rm O/H}) = 8.69$ (Asplund et al. 2021) and adopt a cosmological model with $H_0 = 70 \, {\rm km \, s}^{-1} \, {\rm Mpc}^{-1}$, $\Omega_\Lambda = 0.7$, and $\Omega_{\rm m} = 0.3$.

2. Observations and Data Reductions

2.1. Galaxy Sample

We make a compilation of EMPGs whose metallicities are determined by the direct method in the EMPRESS project and similar studies, which are those of Izotov et al. (2001), Kniazev et al. (2003, 2004), Thuan & Izotov (2005), Izotov & Thuan (2007), Izotov et al. (2009, 2012a, 2012b, 2018, 2019, 2020, 2021), Morales-Luis et al. (2011), Skillman et al. (2013), Hirschauer et al. (2016), Sánchez Almeida et al. (2016), Hsyu et al. (2017), James et al. (2017), and Senchyna & Stark (2019). We select targets for our IFU observations from this compilation by their apparent brightness and visibility on the nights of observations. We prioritize the targets with low

Table 1
Summary of Medium-high Resolution FOCAS-IFU Observations

ID	R.A. (hh:mm:ss)	Decl. (dd:mm:ss)	Redshift	Date of Observation (UT)	Exposure (s)
J0036+0052	00:36:30.40	+00:52:34.71	0.0282	2022 Oct 18	1200
J0057-0941	00:57:57.32	−09:41:19.20	0.0150	2022 Oct 18	1200
J0125+0759	01:25:34.19	+07:59:24.69	0.0098	2022 Oct 18	1200
J0159+0751	01:59:52.75	+07:51:48.80	0.0611	2022 Oct 18	1200
J0228-0210	02:28:02.59	−02:10:55.55	0.0414	2022 Oct 18	1200
SBS 0335-052E[a]	03:37:44.06	−05:02:40.19	0.0135	2021 Nov 25	1200
J0811+4730	08:11:52.12	+47:30:26.24	0.0445	2022 Apr 21	1200
HS 0822+3542[a]	08:25:55.44	+35:32:31.92	0.0023	2021 Dec 14	1200
J0840+4707	08:40:29.90	+47:07:10.30	0.0422	2022 Apr 23	1200
I Zw 18[a]	09:34:02.03	+55:14:28.07	0.0024	2021 Dec 14	180
J0935-0115	09:35:39.20	−01:15:41.41	0.0160	2022 Apr 22	1200
J0943+3326	09:43:32.43	+33:26:58.00	0.0018	2022 Apr 21	1200
DDO 68	09:56:46.05	+28:49:43.78	0.0019	2022 Apr 22	1200
J1016+3754	10:16:24.53	+37:54:45.97	0.0040	2022 Apr 21	1200
Leo P	10:21:45.10	+18:05:17.20	0.0010	2022 Apr 22	1200
J1044+6306[b]	10:44:42.67	+63:06:02.30	0.0033	2022 Apr 23	1200
J1044+0353[a]	10:44:57.79	+03:53:13.15	0.0128	2021 Dec 14	1200
J1234+3901	12:34:15.70	+39:01:16.41	0.1333	2022 Apr 22	1200
J1418+2102	14:18:51.12	+21:02:39.74	0.0086	2022 Apr 22	1200
J1423+2257	14:23:42.88	+22:57:28.80	0.0328	2022 Apr 22	1200
J1452+0241	14:52:55.28	+02:41:01.31	0.0054	2022 Apr 23	1200
J1631+4426[a]	16:31:14.24	+44:26:04.43	0.0313	2021 Aug 14	1200
J1702+2120	17:02:39.88	+21:20:08.91	0.0249	2022 Apr 23	1200
J2104-0035	21:04:55.30	−00:35:22.00	0.0047	2022 Oct 18	1200
J2115-1734[a]	21:15:58.33	−17:34:45.09	0.0230	2021 Aug 14	1200
J2136+0414	21:36:58.81	+04:14:04.31	0.0169	2022 Oct 18	1200
J2302+0049	23:02:10.00	+00:49:38.78	0.0332	2022 Oct 18	1200

Notes.
[a] Paper IX
[b] No detection.

metallicity or possibly complicated dynamical features (e.g., multiple clumps, broad emission lines). Finally, we obtain 32 targets that have a metallicity of $12 + \log(\mathrm{O/H}) \sim 6.86–7.98$. Only three out of the 32 targets have $12 + \log(\mathrm{O/H}) \gtrsim 7.69$, while the others have $12 + \log(\mathrm{O/H}) \lesssim 7.69$, which meets the criteria of EMPGs in the EMPRESS Project.

2.2. Observations

In the EMPRESS 3D project, we conducted observations for the 32 targets over 9 half-nights in 2021–2022. We conducted the observations using FOCAS IFU mounted on the Subaru Telescope. We took science frames using the low-resolution ($R \sim 900$) 300B grism and the mid/high-resolution ($R \sim 7500$) VPH680 grism (hereafter low- and high-resolution data, respectively). The low-resolution data were successfully taken for all 32 targets (see K. Nakajima et al. 2023, in preparation). Paper IX reports the first six targets with high-resolution data taken in 2021 that have enabled us to study the dynamics of EMPGs. In 2022, we further obtained high-resolution data for 20 targets. In total, we obtained low-resolution data for 32 objects and high-resolution data for 26 ($=6 + 20$) targets.

Here we describe the observations in 2022 during which we observed 21 targets. Because of the relatively high redshift of J1234+3901, we used the VPH850 grim ($R \sim 1350$) to take the high-resolution data. The observation nights were on 2022 April 20, 21, 22, and October 17, with typical seeing sizes of $0\farcs6$, $0\farcs5$, $0\farcs8$, and $0\farcs4$, respectively. There were thin clouds at

the beginning of the observations on April 21. On the other nights, the sky was clear. We took calibration data for flat fielding and wavelength calibration at the beginning of observations. We observed standard stars at the beginning or at the end of the observations. We found no detection in the high-resolution data of J1044+6306 and successfully obtained high-resolution data for 20($=21 − 1$) targets. The observations are summarized in Table 1.

2.3. Data Reductions

We use a reduction pipeline software of FOCAS IFU (Ozaki et al. 2020) based on PyRAF (Tody 1986) and Astropy (Astropy Collaboration et al. 2013, 2018, 2022). The software performs bias subtraction, flat fielding, wavelength calibration, cosmic-ray removal, and flux calibration. The software outputs three-dimensional (3D) data cubes of IFS with and without sky background subtraction. The 3D data cubes cover a field of view (FoV) of $13\farcs5 \times 10\arcsec$ with 64×23 spaxels, which corresponds to a pixel scale of $0\farcs215$ and $0\farcs435\,\mathrm{pix}^{-1}$ in the x- and y-axes, respectively. For the low-resolution data, the 3D data cubes cover the wavelengths of 3500–8000 Å. For the high-resolution data, the 3D data cubes cover the wavelengths of 6500–7500 and 6000–10000 Å for the VPH650 and VPH850 grisms, respectively. We estimate the flux uncertainties containing read-out noises and photon noises of sky and object emissions.

2.4. Deblending of Spatial Components

Our data includes EMPGs that have multiple spatial components as shown in the photometric images. The multiple components can also be seen in the Hα flux maps derived from our IFU data (see Figure 1(a) and Section 3.2). In this study, we aim to discuss the properties of individual components exploiting the spatial resolution of the IFU data. We define the components based on the morphology of the Hα flux map using the tool of source detection and deblending in Photutils, an Astropy package. We carefully choose the flux threshold to include only components that have photometric counterparts in the SDSS catalog. Twenty targets appear to have only one component of our interest. From five EMPGs, which are J0057-0941, J2104-0035, J2115-1734, DDO 68, and I Zw 18, we extract two components. For J0125 +0759, we extract three components. We label the components with suffices, where the brightest one is labeled #1. For I Zw 18, we separate I Zw 18-NW and I Zw 18-SE. For DDO 68, we use labels #2 and #3 consistent with the notations used in previous studies (e.g., Pustilnik et al. 2005). Although the origin of the multiple components in one system is debatable, we treat each component as an individual EMPG in this study, which means our sample consists of 33 $(=20 + 5 \times 2 + 3)$ EMPGs in total.

3. Analyses and Results

3.1. Gas Mass Fraction

Gas mass surface density ($\Sigma_{\rm gas}$) can be estimated from the star formation rate (SFR) surface density adopting the Kennicutt–Schmidt law (Kennicutt 1998):

$$\Sigma_{\rm SFR} = (2.5 \pm 0.7) \times 10^{-4}$$
$$\left(\frac{\Sigma_{\rm gas}}{1\,M_\odot\,{\rm pc}^{-1}} \right)^{1.4 \pm 0.15} M_\odot\,{\rm yr}^{-1}\,{\rm kpc}^{-2}. \quad (1)$$

We estimate the SFR surface density ($\Sigma_{\rm SFR}$) from the Hα flux using the relation from Kennicutt (1998), assuming the initial mass function (IMF) of Chabrier (2003):

$$\text{SFR}\,[M_\odot\,{\rm yr}^{-1}] = 4.4 \times 10^{-42}\,L({\rm H}\alpha)\,[{\rm erg\,s}^{-1}]. \quad (2)$$

We fit a Gaussian profile to the spectrum of emission line using the low-resolution data, which offers a better signal-to-noise ratio (S/N) for the Hα lines.

Gas mass fraction is defined as the ratio between the gas mass and the total baryonic mass within one effective radius:

$$f_{\rm gas} = \frac{M_{\rm gas}(r<r_{\rm e})}{M_{\rm gas}(r<r_{\rm e}) + M_*(r<r_{\rm e})}. \quad (3)$$

We sum up $\Sigma_{\rm gas}$ for the spaxels within $r_{\rm e}$ to obtain $M_{\rm gas}(r < r_{\rm e})$. The value of $r_{\rm e}$ is derived by fitting a Sérsic profile to the Hα flux maps. The fitting procedure is integrated into the rotation disk models for the 15 spatially resolved EMPGs (see Section 3.2) and conducted separately using galfit (Peng et al. 2002, 2010) for the other $18(=33 - 15)$ EMPGs. For the stellar masses, there are 15 EMPGs whose stellar masses are measured in previous studies (Table 2). To estimate the stellar masses for the other EMPGs, we first obtain the i-band magnitudes for all 33 EMPGs from the SDSS catalog. We obtain an average mass-to-light ratio of 0.12 between the stellar

mass and i-band magnitude using the 15 EMPGs with known stellar masses. For the other $18(=33 - 15)$ EMPGs, we derive the stellar masses from the absolute i-band magnitudes assuming the mass-to-light ratio. We assume the effective radius of the stellar component ($r_{\rm e,*}$) can be approximated by $r_{\rm e}$ and estimate $M_*(r < r_{\rm e})$ by dividing the stellar masses by 2. We check the possible systematic errors given by our analysis method. We confirm that the gas mass fraction is consistent between the 15 galaxies whose stellar masses are derived from a fixed mass-to-light ratio and the rest of the sample. Since some EMPGs are identified from multiple components in one FoV (Section 2.4), we ensure the consistency between the i-band aperture and the spaxels used for $M_{\rm gas}(r < r_{\rm e})$. Interestingly, we find the multiple components in one system generally have similar $f_{\rm gas}$, implying that the multiple components may have similar star formation histories.

We evaluate the uncertainty of $M_*(r < r_{\rm e})$ assuming $r_{\rm e,*}$ ranges from $r_{\rm e}/2$ to $2r_{\rm e}$. We take the 0.3 dex scatter of Kennicutt–Schmidt law as the uncertainty of $M_{\rm gas}(r < r_{\rm e})$. The calibration from Kennicutt (1998) may underestimate the gas mass for metal-poor galaxies (e.g., Shi et al. 2014). Therefore, we add an upper error of 1 dex to our estimation of $M_{\rm gas}(r < r_{\rm e})$ following Paper IX. We propagate these uncertainties to obtain the error of $f_{\rm gas}$. The results are summarized in Table 2. In the bottom panels of Figure 2, we show $f_{\rm gas}$ as a function of stellar mass and metallicity. We obtain a median value of $f_{\rm gas} \sim 0.9$ larger than those of more massive galaxies in Barat et al. (2020), which suggests EMPGs are likely gas-rich systems.

The average and standard deviation of $f_{\rm gas}$ is 0.8 and 0.2, respectively. Six galaxies (J0057-0941, J0943+3326, J2104-0035, I Zw 18-NW/-SE, and Leo P) are 1σ below the average having $f_{\rm gas} < 0.6$. One possibility of finding low $f_{\rm gas}$ is the existence of an old stellar population (e.g., I Zw 18; Vaduvescu et al. 2005; Aloisi et al. 2007). We find Leo P may be relatively gas deficient with $f_{\rm gas} = 0.12^{+0.75}_{-0.08}$, although with a large uncertainty. Bernstein-Cooper et al. (2014) conducted H I observations and obtained $f_{\rm gas} \sim 0.7$ for Leo P. They claim the $f_{\rm gas}$ value is relatively small among EMPGs, which is consistent with our results.

For our EMPGs, we find no clear correlation between $f_{\rm gas}$ and stellar mass or metallicity. It may seem that only high $f_{\rm gas} \gtrsim 0.9$ can be found for EMPGs with $M_* < 10^5\,M_\odot$. However, the fact that apparently bright EMPGs are preferred by our sample selection may lead to selection bias toward high $f_{\rm gas}$ EMPGs. We consider the selection bias by simply assuming a Hα surface brightness of 1×10^{-17} erg s^{-1} cm^{-2} arcsec^{-2}, which is roughly the detection limit of our low-resolution data (Ozaki et al. 2020). We apply the Hα surface brightness to Equations (1) and (2) to derive the limiting $\Sigma_{\rm gas}$ for observable EMPGs. Isobe et al. (2021) measure the effective radius of 27 EMPGs and obtain $r_{\rm e} \sim 200^{+450}_{-110}$ pc. We take the minimum (maximum) value of 100 pc (1000 pc) to integrate the $\Sigma_{\rm gas}$ as the limiting gas mass. Finally, we calculate the limiting $f_{\rm gas}$ as a function of M_* using Equation (3). In the bottom-left panel of Figure 2, we show two gray regions below the limit $f_{\rm gas}$, where the lighter (darker) colors correspond to the case of minimum (maximum) $r_{\rm e}$ values. We find the correlation between $f_{\rm gas}$ and M_* is possibly biased below $10^6\,M_\odot$. On the other hand, there is no clear correlation between $f_{\rm gas}$ and M_* above $10^6\,M_\odot$.
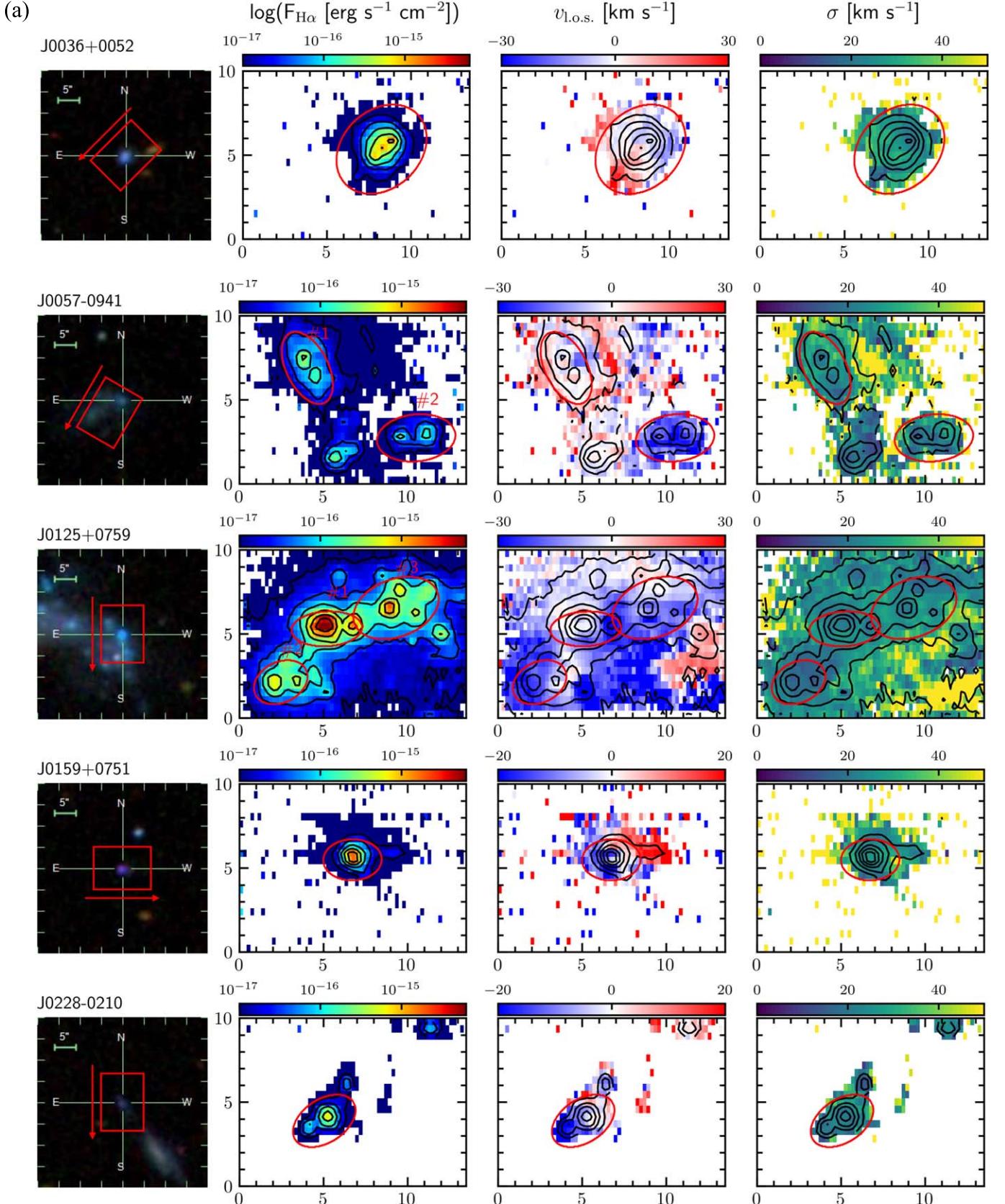
Figure 1. (a) From left to right: SDSS cutout, Hα flux map, line-of-sight velocity map, and velocity dispersion map for each EMPG whose high-resolution data is reported in this study and Paper IX. Spaxels with S/N (Hα) >3 are plotted. The red rectangle on the SDSS cutout indicates the pointing position of our IFU observations while the arrow indicates the direction of the x-axis. The x- and y-axes are presented in arcsec. The black contours represent the Hα flux in the range of $\log(F_{H\alpha}/\mathrm{erg\ s^{-1}\ cm^{-2}}) = -17$ to -14.5 with a step of 0.5 dex. The red circles highlight the apertures we obtained by source detection (see Section 2.4). Within the apertures, we fit disk rotation models. (b) The global Toomre Q parameter as a function of M_* (left) and metallicity (right). The red triangles indicate the four EMPGs with large global Toomre Q values that are out of the y-axis range. All of the EMPGs shown in this plot have $Q > 1$.
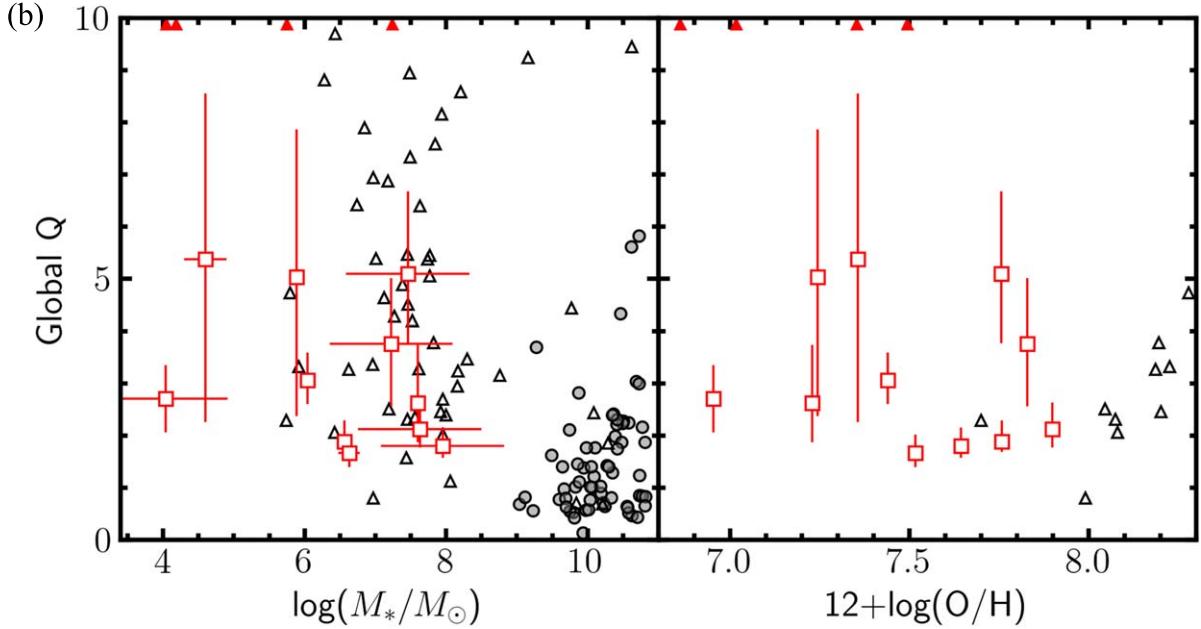
Figure 1. (Continued.)

3.2. Gas Kinematics

We derive the kinematical properties of our EMPGs from the Hα lines. The spatial distribution of line-of-sight velocity ($v_{\text{l.o.s.}}$) and velocity dispersion (σ) can be derived by fitting a Gaussian profile to each spaxel of the high-resolution data. For the line-of-sight velocity, we derive the velocity from the central wavelength ($\lambda_{\text{H}\alpha}$):

$$v_{\text{l.o.s.}} = c(\lambda_{\text{H}\alpha} - \lambda_0 - \lambda_{\text{shift}})/\lambda_0, \qquad (4)$$

where λ_0 represents the systemic wavelength. For EMPGs that can be fitted by a rotation disk model (see below), λ_0 is the observed wavelength at the center of the disk model. Otherwise, we adopt the central wavelength in the spaxel where the flux of Hα is the largest among all the spaxels. The value of λ_{shift} is given by the slit-width effect that is caused by a flux gradient parallel to the wavelength direction (see Section 3.2 in Paper IX) and c is the speed of light. For the velocity dispersion, we subtract the instrumental broadening (σ_{inst}) from the line width ($\sigma_{\text{H}\alpha}$):

$$\sigma = \sqrt{\sigma_{\text{H}\alpha}^2 - \sigma_{\text{inst}}^2}. \qquad (5)$$

We estimate a typical value of $\sigma_{\text{inst}} = 17 \pm 2 \, \text{km s}^{-1}$ from the line widths of unresolved skylines, where the uncertainty is the standard deviation of σ_{inst} from different spaxels. We show the Hα flux, velocity, and dispersion maps in Figures 1(a) and (b).

Assuming that the line-of-sight velocities are given by disk rotation, we can derive the maximum rotation velocity (v_{rot}) that can be compared to the velocity dispersion to study how EMPGs are dynamically supported. We model the disk rotation using the software GalPak^{3D} (Bouché et al. 2015). We follow the method described in Paper IX to prepare the input data cube. Because GalPak^{3D} requires the input data cube to have the same pixel scale on the x- and y-axes, we interpolate the data cube on the y-axis to have a pixel scale of $\sim 0\farcs 217 \, \text{pix}^{-1}$. We also correct the wavelength by the slit-width effect. We

only use the spaxels within the apertures that are determined by the source detection procedure in Section 2.4 and mask out the rest of the 3D data cube. We mask out the spaxels with S/N (Hα) <3. We calculate the 84th percentile of σ for the spaxels left and mask out the spaxels with σ larger than the 84 percentile because the spaxels with large σ could be strongly turbulent (Egorov et al. 2021). We then fit the 3D data cube by a thick disk model. Specifically, we choose a disk model with a disk height equal to one-third of the effective radius. The Hα surface brightness is an exponential function of radius, i.e., a Sérsic profile with a Sérsic index of 1. We choose the arctan rotation curve with two parameters, maximum rotation velocity (v_{rot}) and turnover radius (r_v). The disk model consists of 10 parameters in total, which are x- and y-coordinates of the center, total flux, effective radius (r_e), r_v, inclination (i), position angle, systemic velocity, v_{rot}, and intrinsic dispersion (σ_0). The intrinsic dispersion is free from the broadening given by the instrument, the local isotropic velocity dispersion driven by disk self-gravity, and the mixture of the line-of-sight velocities due to the disk thickness (Bouché et al. 2015). We fit the disk model to all 33 EMPGs. For EMPGs with compact sizes, we find the best-fit r_e is below the seeing size, in which case the parameters are not well constrained (see Section 4.3 in Bouché et al. 2015). We thus only report nine spatially resolved EMPGs with reliable v_{max} and σ_0 measurements that are shown in Table 2. The measurements of v_{rot} and σ_0 for the six EMPGs given by Paper IX are also included. We obtain average values of $v_{\text{rot}} = 15 \, \text{km s}^{-1}$ and $\sigma_0 = 27 \, \text{km s}^{-1}$, with standard errors of 3 and 10 km s^{-1}, respectively. We confirm that all 15(=9 + 6) EMPGs have $v_{\text{rot}}/\sigma_0 < 1$, indicating that they may be dispersion dominated (Förster Schreiber et al. 2009).

We show v_{rot}/σ_0 as a function of M_* and metallicity in the top panels of Figure 2. We also include the v_{rot}/σ_0 values of dwarf galaxies investigated by the DYNAMO survey (Green et al. 2014) and the SHαDE survey (Barat et al. 2020) as comparisons. Their results are also derived from the ionized gas. We show that EMPGs have a low v_{rot}/σ_0, which is smaller
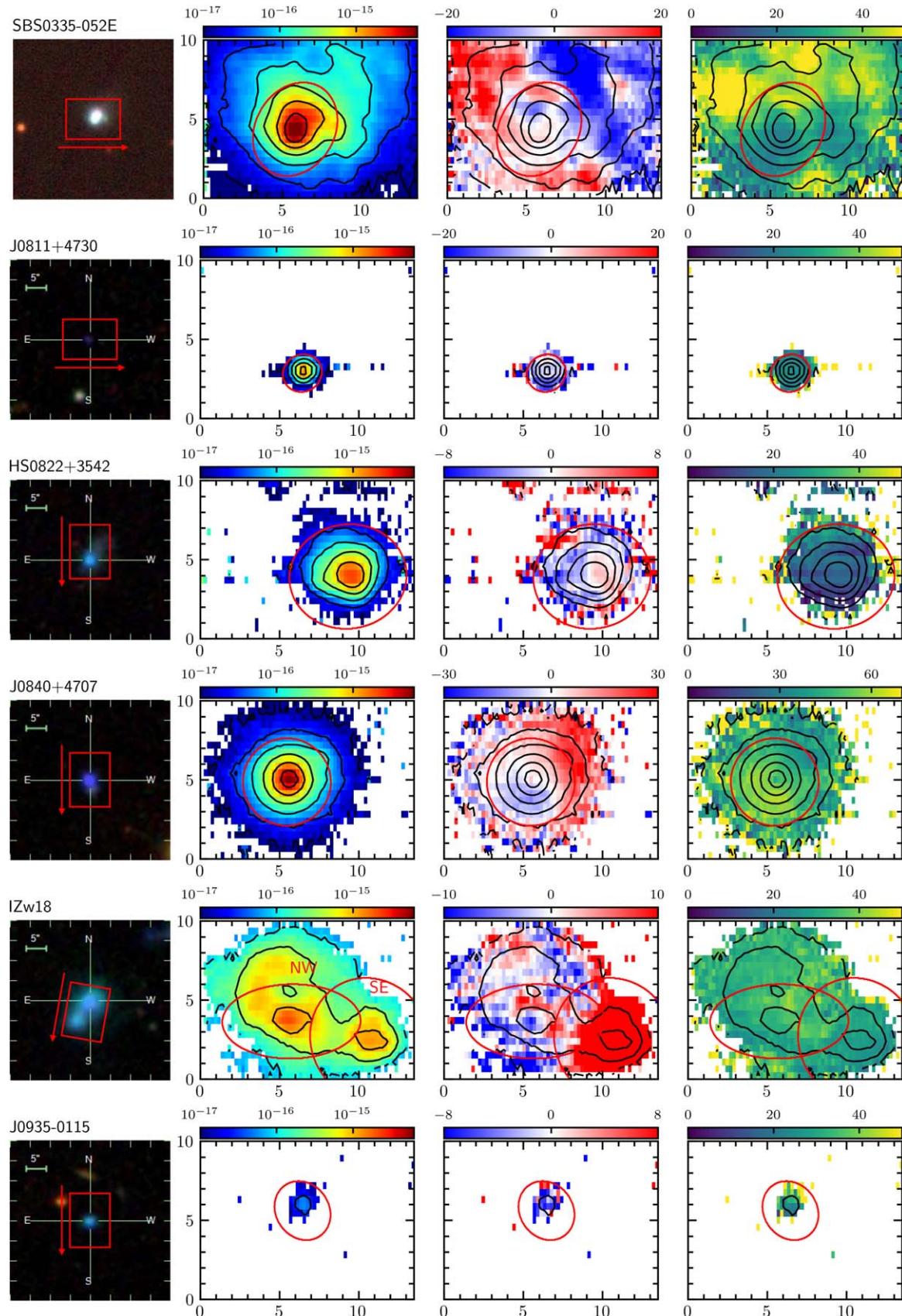
**Figure 1.** (Continued.)
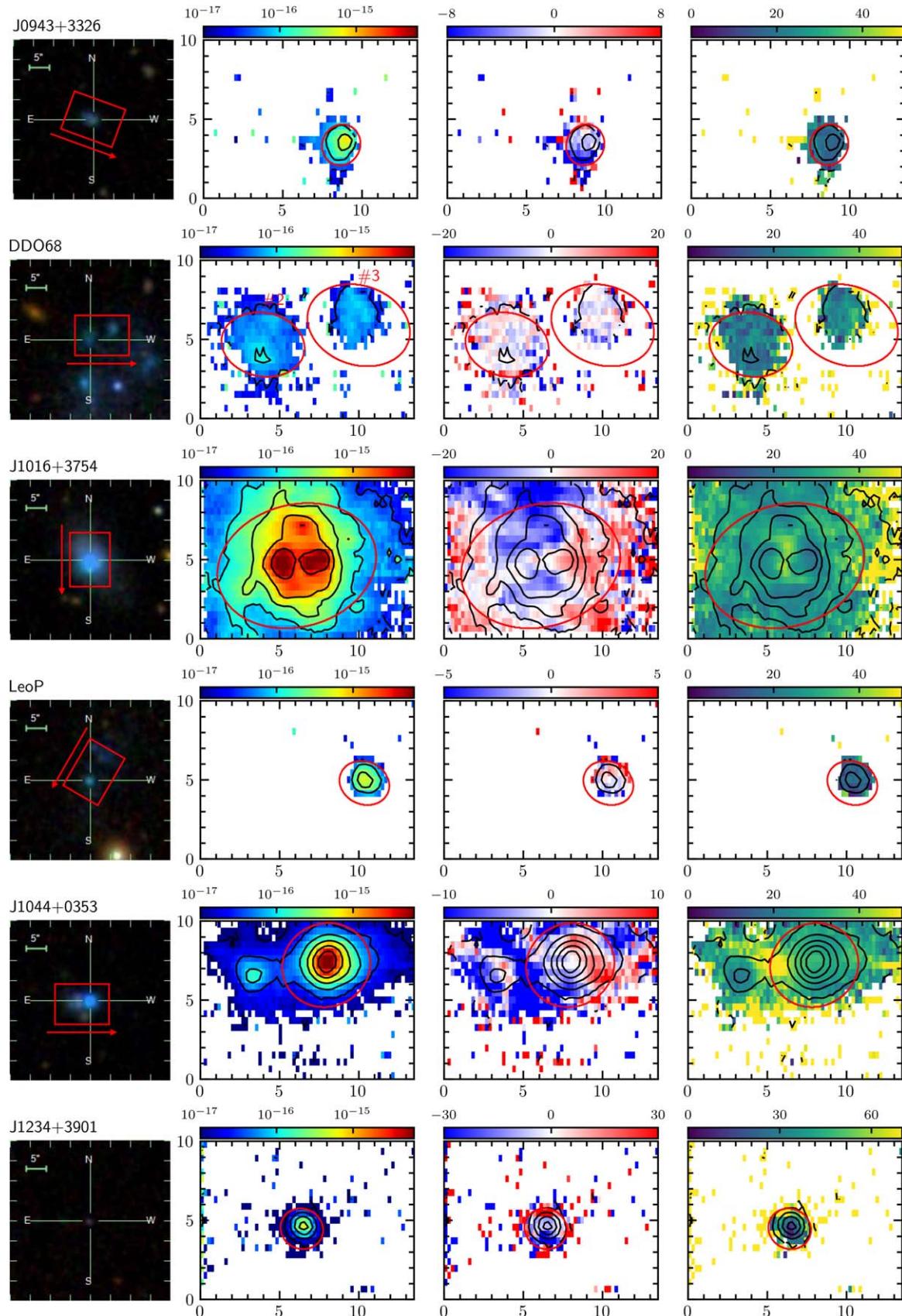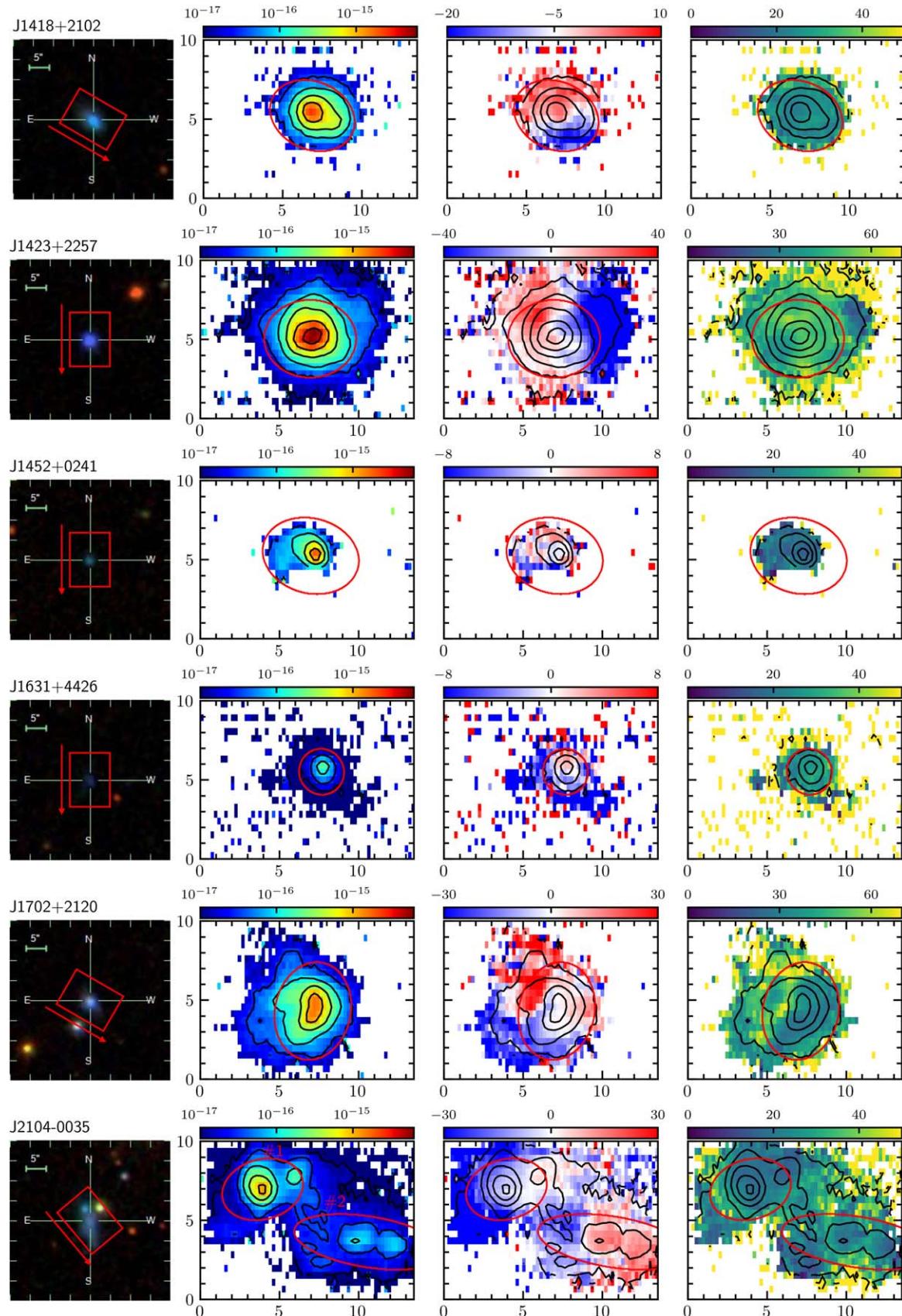
**Figure 1.** (Continued.)
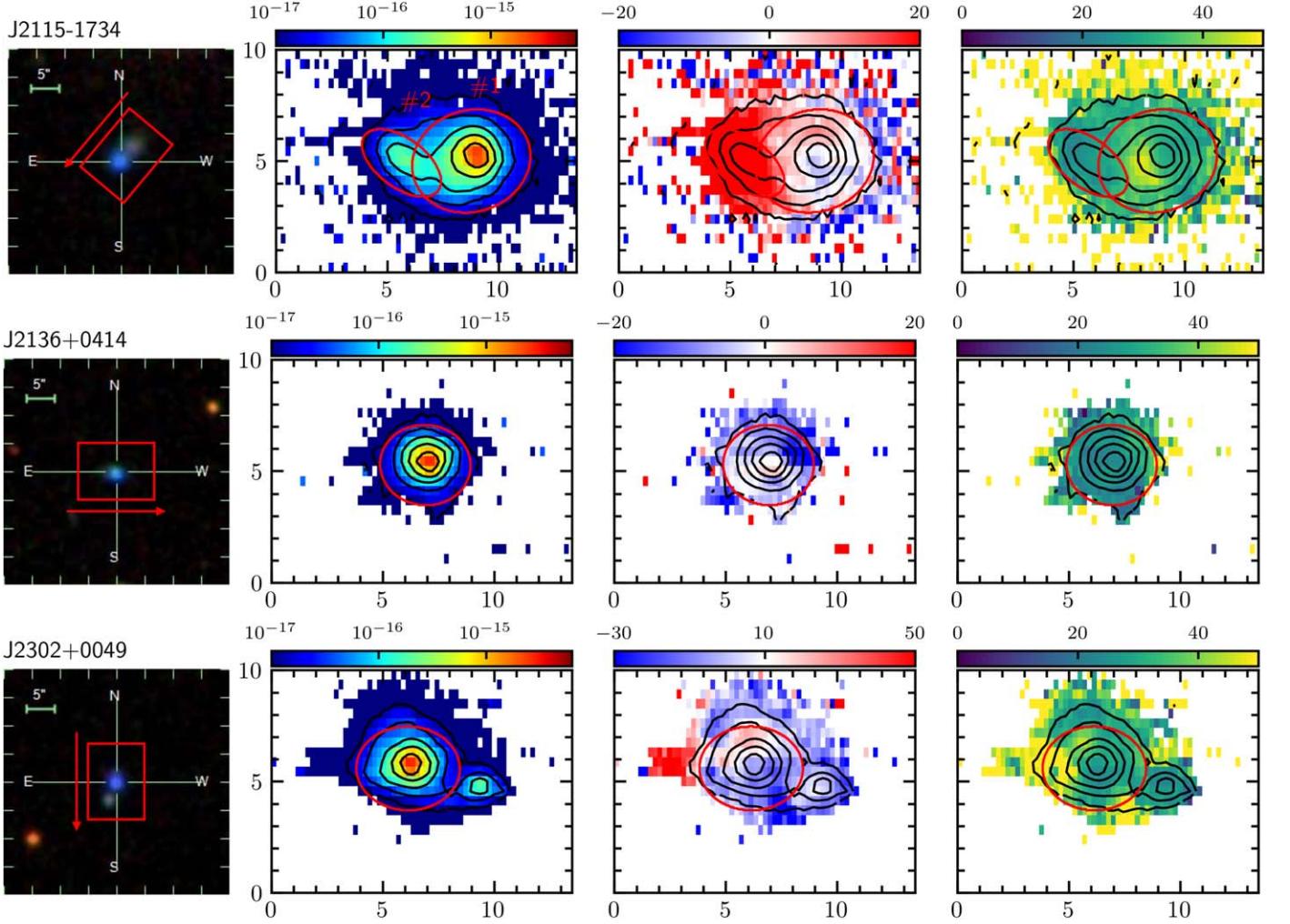
Figure 1. (Continued.)

Figure 1. (Continued.)

than those of more massive galaxies and comparable to those of low-mass galaxies.

4. Discussion

4.1. v_{rot}/σ_0 Scaling Relations for EMPGs

Galaxies that reside in low-mass DM halos with shallow gravitational potential are more likely to have low v_{rot}/σ_0. Our 15 EMPGs clearly fall into the regime of dispersion-dominated galaxies having an average of $v_{rot}/\sigma_0 = 0.48 \pm 0.28$. As a comparison, the dwarf galaxies ($10^6 < M_* < 10^9\,M_\odot$) studied in Barat et al. (2020) have an average v_{rot}/σ_0 of 0.84. de los Reyes et al. (2023) also obtain low $v_{rot}/\sigma_0 \lesssim 2$ based on the stellar kinematics of local dwarf galaxies ($10^7 < M_* < 10^9\,M_\odot$) and suggest a positive correlation that is independent of environmental effect. We note that EMPGs are selected with low-metallicity and high sSFR ($\log(\text{sSFR}/\text{Gyr}^{-1}) \sim 1$–3; Kojima et al. 2020) compared to the more uniform samples used by Barat et al. (2020) and de los Reyes et al. (2023). It is curious whether the correlation between v_{rot}/σ_0 and M_* is still present for EMPGs that undergo recent star formation. We divide our sample into two stellar mass bins of $M_* < 10^6\,M_\odot$ and $>10^6\,M_\odot$. We obtain $v_{rot}/\sigma_0 = 0.24 \pm 0.16$ and 0.64 ± 0.22, respectively. As

shown in Figure 2, EMPGs with $M_* < 10^6\,M_\odot$ have smaller v_{rot}/σ_0 than those with $M_* > 10^6\,M_\odot$ with at least 1σ significance. For the six galaxies (HS 0822+3542, DDO 68-#2, -#3, Leo P, J1452+0241, and J1631+4426) with $M_* < 10^6\,M_\odot$, we only find a weak velocity gradient in the velocity maps shown in Figure 1(a), consistent with the conclusion that they may not present any rotation.

In this study, we present a reasonably large sample of EMPGs to investigate the correlation between v_{rot}/σ_0 and metallicity. We find a positive correlation as shown in the top-right panel of Figure 2 with a Pearson coefficient of 0.50 ($p = 0.06$). The small v_{rot}/σ_0 for the EMPGs with the smallest metallicity probably suggests that they are experiencing the first star formation activity due to gas inflow. To test this hypothesis, we include the classification of EMPGs based on the spatial distribution of metallicity that is taken from a companion paper. K. Nakajima et al. (2023, in preparation) divide our EMPGs into four categories: Category A with a metal-poor region in the center and relatively metal enriched around it, Category B with only a metal-poor region, Category C in the transitioned phase, and the unresolved Category D. One scenario to explain the metallicity distribution of Category A EMPGs is that cold gas inflow accretes directly into the center of EMPGs (e.g., Sánchez Almeida et al. 2014;

Table 2
Summary of Galaxy Properties

ID	$\log M_*$ (log $M_\odot$)	References	logSFR (log $M_\odot$ yr^{-1})	$12 + \log(\mathrm{O/H})$	$v_{\rm rot}$ (km s^{-1})	σ_0 (km s^{-1})	$v_{\rm rot}/\sigma_0$	$f_{\rm gas}$	Q
(1)	(2)	(3)	(4)	(5)	(6)	(7)	(8)	(9)	(10)
J0036+0052	7.22 ± 0.87	⋯	-1.57	7.83	12.8 ± 1.9	24.6 ± 1.9	0.52 ± 0.09	$0.72^{+0.27}_{-0.29}$	$3.76^{+1.25}_{-1.20}$
J0057-0941-#1	6.50 ± 0.87	⋯	-2.67	7.33	⋯	⋯	⋯	$0.61^{+0.38}_{-0.29}$	⋯
J0057-0941-#2	6.87 ± 0.87	⋯	-2.63	7.56	⋯	⋯	⋯	$0.45^{+0.52}_{-0.26}$	⋯
J0125+0759-#1	6.24 ± 0.87	⋯	-1.63	7.47	⋯	⋯	⋯	$0.93^{+0.06}_{-0.13}$	⋯
J0125+0759-#2	5.33 ± 0.87	⋯	-2.60	7.45	⋯	⋯	⋯	$0.96^{+0.04}_{-0.09}$	⋯
J0125+0759-#3	5.81 ± 0.87	⋯	-2.13	7.54	⋯	⋯	⋯	$0.94^{+0.05}_{-0.11}$	⋯
J0159+0751	6.69	(1)	-0.68	7.79	⋯	⋯	⋯	$0.99^{+0.01}_{-0.03}$	⋯
J0228-0210	6.87 ± 0.87	⋯	-1.96	7.12	⋯	⋯	⋯	$0.81^{+0.19}_{-0.26}$	⋯
SBS 0335-052E	7.60 ± 0.10	(2)	-0.61	7.23	$19.7 \pm 2.9^{\rm a}$	$27.1 \pm 0.3^{\rm a}$	$0.73 \pm 0.12^{\rm a}$	$0.74^{+0.17{\rm a}}_{-0.51}$	$2.62^{+1.41{\rm a}}_{-0.63}$
J0811+4730	6.24 ± 0.33	(3)	-2.78	7.12	⋯	⋯	⋯	$0.78^{+0.22}_{-0.27}$	⋯
HS 0822+3542	4.60 ± 0.30	(4)	-2.69	7.36	$4.5 \pm 2.9^{\rm a}$	$16.6 \pm 0.5^{\rm a}$	$0.27 \pm 0.17^{\rm a}$	$0.97^{+0.03{\rm a}}_{-0.07}$	$5.40^{+3.38{\rm a}}_{-3.36}$
J0840+4707	7.95 ± 0.87	⋯	-0.11	7.64	45.0 ± 2.6	51.3 ± 1.9	0.88 ± 0.06	$0.89^{+0.11}_{-0.18}$	$1.80^{+0.35}_{-0.23}$
I Zw 18-NW	$7.24^{\rm a}$	⋯	-1.99	7.35	$6.6 \pm 2.9^{\rm a}$	$22.9 \pm 0.4^{\rm a}$	$0.29 \pm 0.13^{\rm a}$	$0.42^{+0.37{\rm a}}_{-0.32}$	$11.61^{+6.45{\rm a}}_{-6.85}$
I Zw 18-SE	$6.40^{\rm a}$	⋯	-2.63	7.04	⋯	⋯	⋯	$0.51^{+0.47}_{-0.28}$	⋯
J0935-0115	6.16 ± 0.14	(5)	-1.55	7.13	⋯	⋯	⋯	$0.96^{+0.04}_{-0.09}$	⋯
J0943+3326	5.56 ± 0.30	(6)	-3.66	7.09	⋯	⋯	⋯	$0.52^{+0.47}_{-0.28}$	⋯
DDO 68-#2	4.03 ± 0.88	⋯	-3.44	6.95	10.0 ± 2.1	18.8 ± 2.0	0.53 ± 0.13	$0.99^{+0.01}_{-0.03}$	$2.71^{+0.65}_{-0.64}$
DDO 68-#3	4.04 ± 0.88	⋯	-3.61	6.86	1.5 ± 2.1	22.4 ± 2.0	0.07 ± 0.10	$0.98^{+0.02}_{-0.04}$	$21.05^{+29.46}_{-29.45}$
J1016+3754	6.59 ± 0.87	⋯	-2.03	7.88	⋯	⋯	⋯	$0.70^{+0.29}_{-0.29}$	⋯
Leo P	5.75 ± 0.09	(7)	-4.28	7.02	2.7 ± 2.2	15.9 ± 1.9	0.17 ± 0.14	$0.12^{+0.75}_{-0.08}$	$67.92^{+55.44}_{-75.03}$
J1044+0353	6.04 ± 0.07	(5)	-1.04	7.44	$14.8 \pm 4.2^{\rm a}$	$31.4 \pm 0.3^{\rm a}$	$0.47 \pm 0.14^{\rm a}$	$0.98^{+0.01{\rm a}}_{-0.09}$	$3.07^{+0.96{\rm a}}_{-0.92}$
J1234+3901	7.13 ± 0.30	(3)	-0.65	7.08	⋯	⋯	⋯	$0.98^{+0.02}_{-0.05}$	⋯
J1418+2102	6.63 ± 0.15	(8)	-1.38	7.52	22.6 ± 2.1	23.9 ± 1.9	0.95 ± 0.12	$0.90^{+0.10}_{-0.18}$	$1.66^{+0.36}_{-0.26}$
J1423+2257	7.63 ± 0.87	⋯	-0.66	7.90	34.6 ± 1.9	43.9 ± 1.9	0.79 ± 0.06	$0.84^{+0.15}_{-0.23}$	$2.13^{+0.51}_{-0.36}$
J1452+0241	4.18 ± 0.14	(5)	-2.69	7.49	1.1 ± 2.0	17.5 ± 1.9	0.06 ± 0.11	$0.99^{+0.00}_{-0.01}$	$22.04^{+38.40}_{-38.40}$
J1631+4426	5.89 ± 0.10	(9)	-1.77	7.24	$7.9 \pm 1.8^{\rm a}$	$25.6 \pm 0.3^{\rm a}$	$0.31 \pm 0.08^{\rm a}$	$0.91^{+0.06{\rm a}}_{-0.34}$	$5.01^{+2.11{\rm a}}_{-1.27}$
J1702+2120	7.46 ± 0.87	⋯	-1.09	7.76	11.5 ± 2.0	33.4 ± 1.9	0.34 ± 0.06	$0.81^{+0.19}_{-0.25}$	$5.09^{+1.59}_{-1.33}$
J2104-0035-#1	4.69 ± 0.87	⋯	-2.66	7.20	⋯	⋯	⋯	$0.98^{+0.02}_{-0.04}$	⋯
J2104-0035-#2	6.01 ± 0.87	⋯	-3.63	6.97	⋯	⋯	⋯	$0.36^{+0.60}_{-0.22}$	⋯
J2115-1734-#1	6.56 ± 0.02	(9)	-0.95	7.76	23.4 ± 2.0	29.3 ± 1.9	0.80 ± 0.09	$0.97^{+0.03}_{-0.07}$	$1.83^{+0.23}_{-0.20}$
J2115-1734-#2	7.17 ± 0.87	⋯	-1.62	7.83	⋯	⋯	⋯	$0.94^{+0.04{\rm a}}_{-0.18}$	$1.88^{+0.79{\rm a}}_{-0.71}$
J2136+0414	6.53 ± 0.87	⋯	-1.72	7.49	⋯	⋯	⋯	$0.89^{+0.10}_{-0.18}$	⋯
J2302+0049	7.22 ± 0.87	⋯	-0.94	7.62	⋯	⋯	⋯	$0.90^{+0.10}_{-0.17}$	⋯

Notes. Column (1) ID. Column (2) Stellar masses. Column (3) References for the stellar masses: (1) Izotov et al. (2017), (2) Pustilnik et al. (2004), (3) Izotov et al. (2012a), (4) Annibali et al. (2013), (5) Xu et al. (2022), (6) Hirschauer et al. (2016), (7) McQuinn et al. (2015), (8) Filho et al. (2013), (9) Kojima et al. (2020). Column (4) SFR calculated from the dust attenuation corrected Hα line fluxes. The relative uncertainties are smaller than 1% in linear scale. Column (5) Metallicity estimated from the R3 index of the integrated [O III] and Hβ flux. Columns (6)–(8) Maximum rotation velocity, intrinsic velocity dispersion, and their ratio given by the best-fit rotation disk model. Column (9) Gas mass fraction. Column (10) Global Toomre Q parameter.
[a] Paper IX.

K. Nakajima et al. 2023, in preparation). In Figure 3, we show $v_{\rm rot}/\sigma_0$ as a function of metallicity with each EMPG color coded by the categories. Surprisingly, Category A EMPGs have a $v_{\rm rot}/\sigma_0 \sim 0.68 \pm 0.10$ on average, which is larger than that $v_{\rm rot}/\sigma_0 \sim 0.34 \pm 0.08$ for Category B EMPGs, at 1σ significance. In a Category A EMPG, the metal poorest region is surrounded by the metal-enriched regions, which may represent an older stellar population. The older stellar population may have already formed a rotation disk, which is destroyed by the latest gas inflow. For a Category B EMPG, neither an older stellar population nor rotation is detected. Category B EMPGs may undergo their first chemical evolutionary event that could be triggered by gas accretion.

Whether a stable rotation disk can build up in low-mass star-forming galaxies like EMPGs needs to be tested with simulations (see also the discussions in Paper IX). Hopkins et al. (2023)

show that a sufficiently centrally concentrated mass profile is crucial for the initial formation of a disk. However, it is still a difficult task to resolve the profile of mass concentration (e.g., Genzel et al. 2020) for compact low-mass galaxies by observations. High spatial resolution with future observational facilities may help us understand how EMPGs started the recent star formation and why they appear to be dispersion dominated. On the other hand, observations of primordial galaxies at high z (e.g., with JWST) are useful to reveal the relation between dynamics and star formation at the early stage of galaxy formation.

4.2. Mass Profiles

For the 15 EMPGs with $v_{\rm rot}$ and σ_0 measurements, we can compare the radial profile of gas mass and stellar mass to that
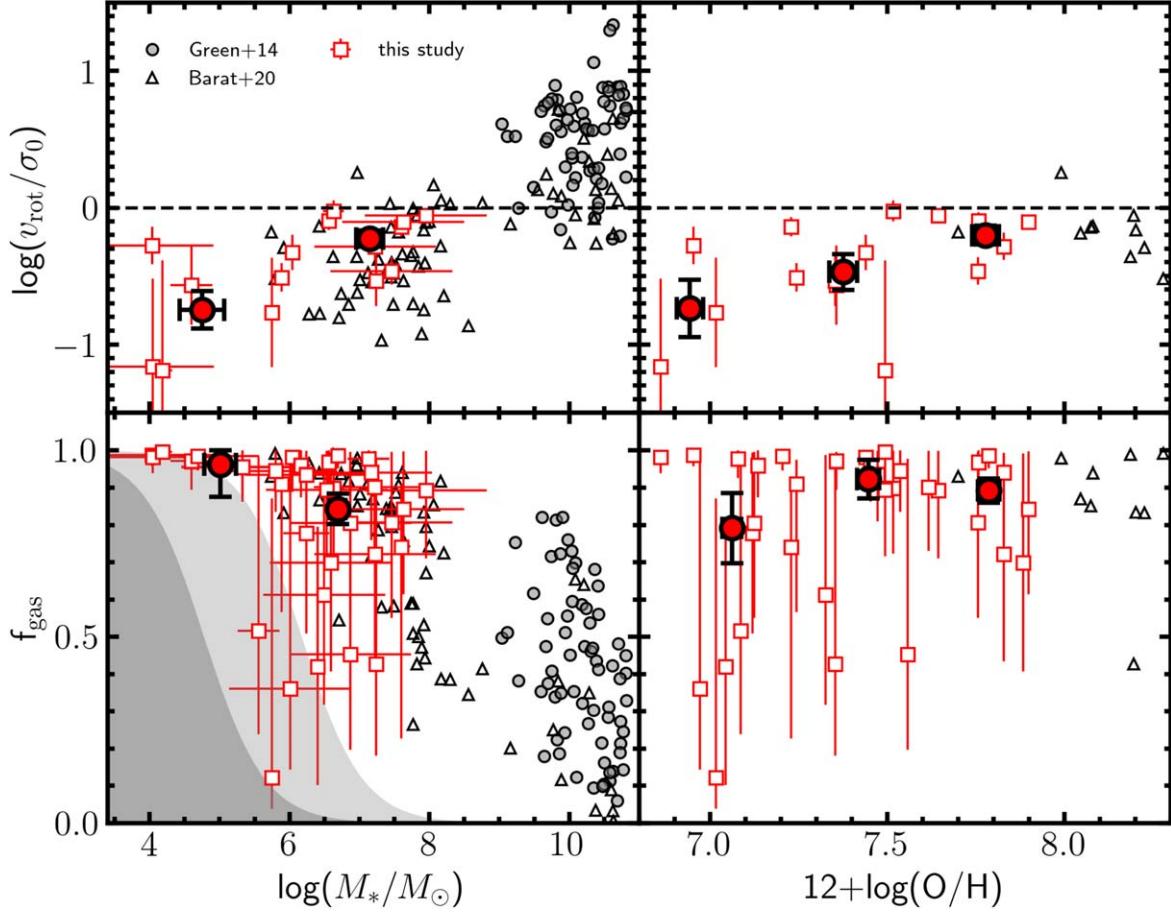
Figure 2. (Top) v_{max}/σ_0 as a function of stellar mass (left) and gas-phase metallicity (right). The red squares represent individual EMPGs while the red circles represent average values in stellar mass (metallicity) bins. The gray circles and triangles indicate data taken from the DYNAMO survey (Green et al. 2014) and the SHαDE survey (Barat et al. 2020), respectively. (Bottom) Same as the top panels but for f_{gas}. We plot the median values with red circles. The gray regions in the bottom-left panel indicate the observational limit for f_{gas} (see Section 3.1).
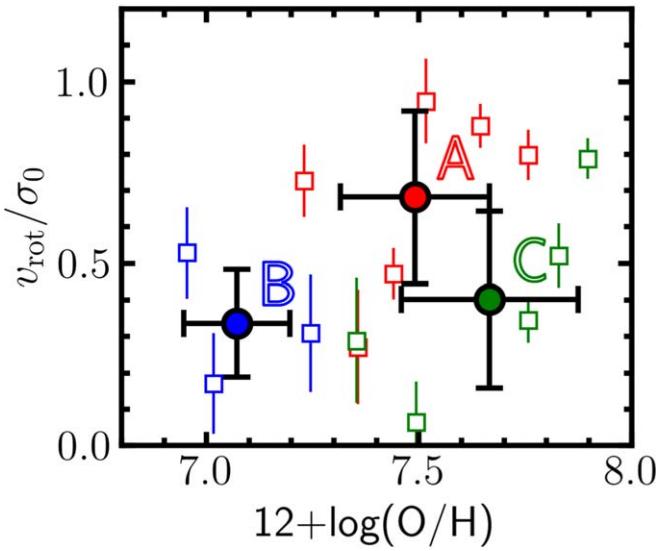
Figure 3. Same as the top-right panel of Figure 2 but color coded by the categories given by K. Nakajima et al. (2023, in preparation). The y-axis is changed to linear scale. Category A EMPGs have surrounding metal-enriched regions that may have come from older stellar populations, while Category B EMPGs only show metal-poor regions given by the recent star formation. Category C EMPGs are possibly in a transition stage.

of the dynamical mass. The dynamical mass enclosed by radius r can be calculated with

$$M_{dyn} = 2.33 \times 10^5 \left(\frac{r}{\mathrm{kpc}}\right)$$
$$\left[\left(\frac{v(r)}{\mathrm{km\ s^{-1}}}\right)^2 + 2\left(\frac{\sigma_0}{\mathrm{km\ s^{-1}}}\right)^2\right] M_\odot. \quad (6)$$

We derive the enclosed dynamical, stellar, gas, and DM mass enclosed by radius r following the procedures in Paper IX. We follow the same procedure as in Paper IX and assume a Sérsic profile and Navarro–Frenk–White (Navarro et al. 1996) profile for the stellar mass and DM mass, respectively. The results are plotted in Figure 4 for 15 EMPGs, including the six EMPGs presented in Paper IX. For 14 out of 15 EMPGs, the mass profile of gas mass contributes to most of the dynamical mass, which is consistent with the large f_{gas} we derived. In general, we find EMPGs are likely puffy gas-rich systems supported by random motion that may be supplied by gas inflow, stellar feedback, or galaxy–galaxy interaction.
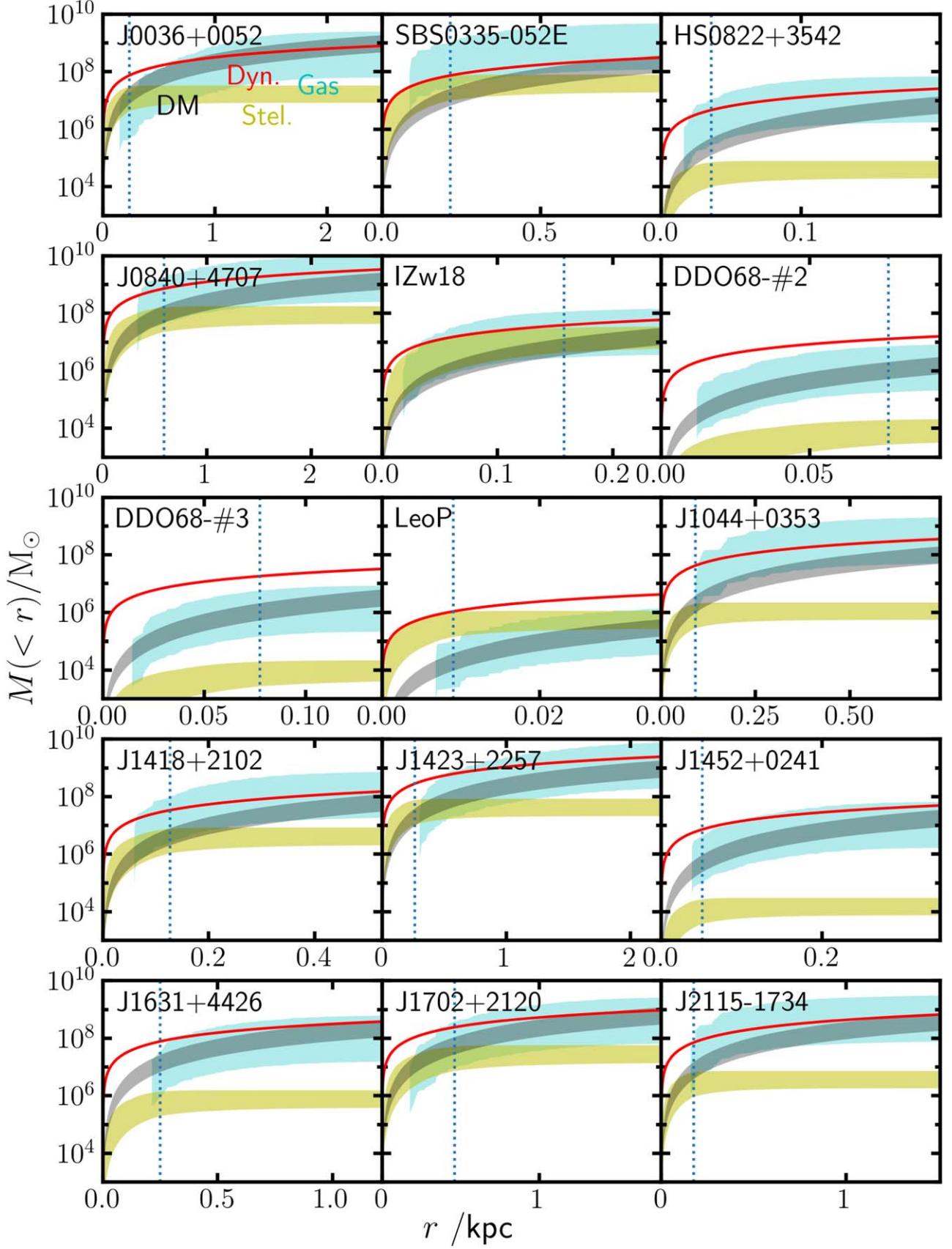
Figure 4. Enclosed mass profiles. The red, yellow, cyan, and black curves represent dynamical, stellar, gas, and DM mass profiles, respectively. The vertical dotted lines show the effective radius of Hα. The edge of the plots corresponds to the outermost radii used for the kinematic analysis.

4.3. Toomre Q Parameter

The Toomre Q parameter is used by many kinematic studies as an indicator of the gravitational stability of disk galaxies (e.g., Genzel et al. 2011). In general, if the Q value of a rotating disk is greater than unity (i.e., $Q > 1$), the disk is thought to be gravitationally stable. On the other hand, if $Q < 1$, the disk is gravitationally unstable. However, it remains an open question on what observable scales the Toomre Q parameter is a reliable indicator of gravitational stability (e.g., Romeo & Agertz 2014). Paper IX also suggests that it is unclear whether this criterion is applicable to EMPGs because they may not have rotating disks. To compare with previous kinematics studies, we calculate the average of Q within a disk that is called the global Q (e.g., Aumer et al. 2010) in the same manner as in Paper IX:

$$Q = \frac{\sigma_0}{v_{\rm rot}} \frac{a}{f_{\rm gas}}, \qquad (7)$$

where the parameter a ranges from 1–2, depending on the gas distribution. We assume $a = \sqrt{2}$, which corresponds to a disk with constant rotational velocity (Genzel et al. 2011). The differences in Toomre Q parameters are less than a factor of 2 if a different value of a is assumed.

We obtain a global Q of 1–70 for 15 EMPGs with a median value of 4. Although all 15 EMPGs have a global Q larger than unity suggestive of a stable disk, the large global Q is inconsistent with the star-forming nature of EMPGs as pointed out in Paper IX. In Figure 1(b), we plot the global Q as a function of stellar mass and metallicity. We find no clear correlation between the global Q and stellar mass or metallicity. It is possible that EMPGs have a large variety of dynamics, or the global Q does not provide a good constraint on the gravitational stability of EMPGs. It is difficult to conclude whether or not EMPGs generally have stable disks without high-resolution observations for both gas and stellar components (e.g., Romeo et al. 2020; Romeo 2020) using next-generation facilities such as ngVLA.

5. Summary

We present the demography of the dynamics and gas mass fraction of 33 EMPGs with metallicities of 0.015–0.195 $Z_\odot$ and low stellar masses of 10^4–$10^8 M_\odot$ in the local universe. We conduct deep optical IFS for low-mass EMPGs with the medium-high resolution ($R = 7500$) grism of the 8 m-Subaru FOCAS IFU instrument by the EMPRESS 3D survey, and investigate the Hα emission of the EMPGs (Section 2). Exploiting the resolution high enough for the low-mass galaxies, we derive gas dynamics with the Hα lines by the fitting of 3D disk models. We obtain an average maximum rotation velocity ($v_{\rm rot}$) of $15 \pm 3 \,{\rm km\,s}^{-1}$ and an average intrinsic velocity dispersion of (σ_0) of $27 \pm 10 \,{\rm km\,s}^{-1}$ for 15 spatially resolved EMPGs out of 33 EMPGs, and find that all 15 EMPGs have $v_{\rm rot}/\sigma_0 < 1$, suggesting dispersion-dominated systems (Section 3.2). There is a clear decreasing trend of $v_{\rm rot}/\sigma_0$ with the decreasing stellar mass and metallicity (Section 4). We derive the gas mass fraction ($f_{\rm gas}$) for all 33 EMPGs, and find no clear dependence on stellar mass and metallicity (Section 3.1). Our results suggest EMPGs are gas-rich dispersion-dominated systems, whose dynamical properties likely depend on the current stellar mass and previous star formation history.

Software: FOCAS IFU pipeline (Ozaki et al. 2020), PyRAF (Tody 1986), Photutils (Bradley et al. 2022), Astropy (Astropy Collaboration et al. 2013, 2018, 2022), GalPaK^{3D} (Bouché et al. 2015), galfit (Peng et al. 2002, 2010).

ORCID iDs

Yi Xu ⓘ https://orcid.org/0000-0002-5768-8235
Masami Ouchi ⓘ https://orcid.org/0000-0002-1049-6658
Yuki Isobe ⓘ https://orcid.org/0000-0001-7730-8634
Kimihiko Nakajima ⓘ https://orcid.org/0000-0003-2965-5070
Shinobu Ozaki ⓘ https://orcid.org/0000-0002-5443-0300
Nicolas F. Bouché ⓘ https://orcid.org/0000-0003-0068-9920
John H. Wise ⓘ https://orcid.org/0000-0003-1173-8847
Eric Emsellem ⓘ https://orcid.org/0000-0002-6155-7166
Haruka Kusakabe ⓘ https://orcid.org/0000-0002-3801-434X
Takashi Hattori ⓘ https://orcid.org/0000-0002-8996-7562
Tohru Nagao ⓘ https://orcid.org/0000-0002-7402-5441
Gen Chiaki ⓘ https://orcid.org/0000-0001-6246-2866
Hajime Fukushima ⓘ https://orcid.org/0000-0002-0547-3208
Yuichi Harikane ⓘ https://orcid.org/0000-0002-6047-430X
Kohei Hayashi ⓘ https://orcid.org/0000-0002-8758-8139
Yutaka Hirai ⓘ https://orcid.org/0000-0002-5661-033X
Ji Hoon Kim ⓘ https://orcid.org/0000-0002-1418-3309
Michael V. Maseda ⓘ https://orcid.org/0000-0003-0695-4414
Kentaro Nagamine ⓘ https://orcid.org/0000-0001-7457-8487
Yuma Sugahara ⓘ https://orcid.org/0000-0001-6958-7856
Hidenobu Yajima ⓘ https://orcid.org/0000-0002-1319-3433
Shohei Aoyama ⓘ https://orcid.org/0000-0002-1005-4120
Seiji Fujimoto ⓘ https://orcid.org/0000-0001-7201-5066
Akio K. Inoue ⓘ https://orcid.org/0000-0002-7779-8677
Takashi Kojima ⓘ https://orcid.org/0000-0001-5780-1886
Yutaka Komiyama ⓘ https://orcid.org/0000-0002-3852-6329
Yusei Koyama ⓘ https://orcid.org/0000-0002-0479-3699
Chien-Hsiu Lee ⓘ https://orcid.org/0000-0003-1700-5740
Ken Mawatari ⓘ https://orcid.org/0000-0003-4985-0201
Takashi J. Moriya ⓘ https://orcid.org/0000-0003-1169-1954
Kentaro Motohara ⓘ https://orcid.org/0000-0002-0724-9146
Kai Murai ⓘ https://orcid.org/0000-0003-2879-1724
Moka Nishigaki ⓘ https://orcid.org/0000-0003-4321-0975
Masato Onodera ⓘ https://orcid.org/0000-0003-3228-7264
Yoshiaki Ono ⓘ https://orcid.org/0000-0001-9011-7605
Michael Rauch ⓘ https://orcid.org/0000-0002-1690-3488
Akihiro Suzuki ⓘ https://orcid.org/0000-0002-7043-6112
Tsutomu T. Takeuchi ⓘ https://orcid.org/0000-0001-8416-7673
Masayuki Umemura ⓘ https://orcid.org/0000-0003-1615-1789
Kiyoto Yabe ⓘ https://orcid.org/0000-0001-6229-4858
Yechi Zhang ⓘ https://orcid.org/0000-0003-3817-8739

References

Aihara, H., AlSayyad, Y., Ando, M., et al. 2019, PASJ, 71, 114
Aloisi, A., Clementini, G., Tosi, M., et al. 2007, ApJL, 667, L151
Annibali, F., Cignoni, M., Tosi, M., et al. 2013, AJ, 146, 144
Asplund, M., Amarsi, A. M., & Grevesse, N. 2021, A&A, 653, A141
Astropy Collaboration, Price-Whelan, A. M., Lim, P. L., et al. 2022, ApJ, 935, 167
Astropy Collaboration, Price-Whelan, A. M., Sipőcz, B. M., et al. 2018, AJ, 156, 123
Astropy Collaboration, Robitaille, T. P., Tollerud, E. J., et al. 2013, A&A, 558, A33
Aumer, M., Burkert, A., Johansson, P. H., & Genzel, R. 2010, ApJ, 719, 1230
Barat, D., D'Eugenio, F., Colless, M., et al. 2020, MNRAS, 498, 5885
Bernstein-Cooper, E. Z., Cannon, J. M., Elson, E. C., et al. 2014, AJ, 148, 35
Blumenthal, G. R., Faber, S. M., Primack, J. R., & Rees, M. J. 1984, Natur, 311, 517
Bouché, N., Carfantan, H., Schroetter, I., Michel-Dansac, L., & Contini, T., 2015 GalPaK 3D: Galaxy parameters and kinematics extraction from 3D data, Astrophysics Source Code Library, ascl:1501.014
Bradley, L., Sipőcz, B., Robitaille, T., et al. 2022, astropy/photutils: v1.5.0, Zenodo, doi:10.5281/zenodo.6825092
Chabrier, G. 2003, PASP, 115, 763
de los Reyes, M. A. C., Kirby, E. N., Zhuang, Z., et al. 2023, ApJ, 951, 52
Dekel, A., Ginzburg, O., Jiang, F., et al. 2020, MNRAS, 493, 4126
Egorov, O. V., Lozinskaya, T. A., Vasiliev, K. I., et al. 2021, MNRAS, 508, 2650
Fall, S. M., & Efstathiou, G. 1980, MNRAS, 193, 189
Filho, M. E., Winkel, B., Sánchez Almeida, J., et al. 2013, A&A, 558, A18
Förster Schreiber, N. M., Genzel, R., Bouché, N., et al. 2009, ApJ, 706, 1364
Genzel, R., Newman, S., Jones, T., et al. 2011, ApJ, 733, 101
Genzel, R., Price, S. H., Übler, H., et al. 2020, ApJ, 902, 98
Green, A. W., Glazebrook, K., McGregor, P. J., et al. 2014, MNRAS, 437, 1070
Hirschauer, A. S., Salzer, J. J., Skillman, E. D., et al. 2016, ApJ, 822, 108
Hopkins, P. F., Gurvich, A. B., Shen, X., et al. 2023, MNRAS, 525, 2241
Hsyu, T., Cooke, R. J., Prochaska, J. X., & Bolte, M. 2017, ApJL, 845, L22
Isobe, Y., Ouchi, M., Kojima, T., et al. 2021, ApJ, 918, 54
Isobe, Y., Ouchi, M., Suzuki, A., et al. 2022, ApJ, 925, 111
Isobe, Y., Ouchi, M., Nakajima, K., et al. 2023, ApJ, 951, 102
Izotov, Y. I., Chaffee, F. H., & Green, R. F. 2001, ApJ, 562, 727
Izotov, Y. I., Guseva, N. G., Fricke, K. J., & Papaderos, P. 2009, A&A, 503, 61
Izotov, Y. I., Schaerer, D., Worseck, G., et al. 2020, MNRAS, 491, 468
Izotov, Y. I., & Thuan, T. X. 2007, ApJ, 665, 1115
Izotov, Y. I., Thuan, T. X., & Guseva, N. G. 2012a, A&A, 546, A122
Izotov, Y. I., Thuan, T. X., & Guseva, N. G. 2017, MNRAS, 471, 548
Izotov, Y. I., Thuan, T. X., & Guseva, N. G. 2019, MNRAS, 483, 5491
Izotov, Y. I., Thuan, T. X., & Guseva, N. G. 2021, MNRAS, 504, 3996
Izotov, Y. I., Thuan, T. X., Guseva, N. G., & Liss, S. E. 2018, MNRAS, 473, 1956
Izotov, Y. I., Thuan, T. X., & Privon, G. 2012b, MNRAS, 427, 1229
James, B. L., Koposov, S. E., Stark, D. P., et al. 2017, MNRAS, 465, 3977
Kennicutt, R. C. J. 1998, ApJ, 498, 541
Kniazev, A. Y., Grebel, E. K., Hao, L., et al. 2003, ApJL, 593, L73
Kniazev, A. Y., Pustilnik, S. A., Grebel, E. K., Lee, H., & Pramskij, A. G. 2004, ApJS, 153, 429
Kojima, T., Ouchi, M., Rauch, M., et al. 2020, ApJ, 898, 142
Kojima, T., Ouchi, M., Rauch, M., et al. 2021, ApJ, 913, 22
Matsumoto, A., Ouchi, M., Nakajima, K., et al. 2022, ApJ, 941, 167
McQuinn, K. B. W., Skillman, E. D., Dolphin, A., et al. 2015, ApJ, 812, 158
Miyazaki, S., Komiyama, Y., Kawanomoto, S., et al. 2018, PASJ, 70, S1
Morales-Luis, A. B., Sánchez Almeida, J., Aguerri, J. A. L., & Muñoz-Tuñón, C. 2011, ApJ, 743, 77
Nakajima, K., Ouchi, M., Xu, Y., et al. 2022, ApJS, 262, 3
Navarro, J. F., Frenk, C. S., & White, S. D. M. 1996, ApJ, 462, 563
Ozaki, S., Fukushima, M., Iwashita, H., et al. 2020, PASJ, 72, 97
Peng, C. Y., Ho, L. C., Impey, C. D., & Rix, H.-W. 2002, AJ, 124, 266
Peng, C. Y., Ho, L. C., Impey, C. D., & Rix, H.-W. 2010, AJ, 139, 2097
Pustilnik, S. A., Kniazev, A. Y., & Pramskij, A. G. 2005, A&A, 443, 91
Pustilnik, S. A., Pramskij, A. G., & Kniazev, A. Y. 2004, A&A, 425, 51
Rizzo, F., Vegetti, S., Fraternali, F., Stacey, H. R., & Powell, D. 2021, MNRAS, 507, 3952
Rizzo, F., Vegetti, S., Powell, D., et al. 2020, Natur, 584, 201
Romeo, A. B. 2020, MNRAS, 491, 4843
Romeo, A. B., & Agertz, O. 2014, MNRAS, 442, 1230
Romeo, A. B., Agertz, O., & Renaud, F. 2020, MNRAS, 499, 5656
Sánchez Almeida, J., Morales-Luis, A. B., Muñoz-Tuñón, C., et al. 2014, ApJ, 783, 45
Sánchez Almeida, J., Pérez-Montero, E., Morales-Luis, A. B., et al. 2016, ApJ, 819, 110
Senchyna, P., & Stark, D. P. 2019, MNRAS, 484, 1270
Shi, Y., Armus, L., Helou, G., et al. 2014, Natur, 514, 335
Skillman, E. D., Salzer, J. J., Berg, D. A., et al. 2013, AJ, 146, 3
Thuan, T. X., Guseva, N. G., & Izotov, Y. I. 2022, MNRAS, 516, L81
Thuan, T. X., & Izotov, Y. I. 2005, ApJS, 161, 240
Tody, D. 1986, Proc. SPIE, 627, 733
Tokuoka, T., Inoue, A. K., Hashimoto, T., et al. 2022, ApJL, 933, L19
Umeda, H., Ouchi, M., Nakajima, K., et al. 2022, ApJ, 930, 37
Vaduvescu, O., McCall, M. L., Richer, M. G., & Fingerhut, R. L. 2005, AJ, 130, 1593
White, S. D. M., & Rees, M. J. 1978, MNRAS, 183, 341
Xu, Y., Ouchi, M., Rauch, M., et al. 2022, ApJ, 929, 134